



Recurrent slow slip events as a barrier to the northward rupture propagation of the 2016 Pedernales earthquake (Central Ecuador)

Sandro Vaca^{a,b,*}, Martin Vallée^a, Jean-Mathieu Nocquet^c, Jean Battaglia^d, Marc Régnier^c

^a Institut de Physique du Globe de Paris, Sorbonne Paris Cité, Université Paris Diderot, UMR 7154 CNRS, Paris, France

^b Instituto Geofísico-Escuela Politécnica Nacional, Quito, Ecuador

^c Geozur, IRD, CNRS, Observatoire de la Côte d'Azur, Université de Nice Sophia-Antipolis, Valbonne, France

^d Laboratoire Magmas et Volcans, Université Blaise Pascal-CNRS-IRD, Clermont-Ferrand, France

ARTICLE INFO

Keywords:

Subduction
Slow slip event
Seismic swarm
Interseismic coupling
Pedernales earthquake
Propagation barrier

ABSTRACT

The northern Ecuador segment of the Nazca/South America subduction zone shows spatially heterogeneous interseismic coupling. Two highly coupled zones (0.4° S– 0.35° N and 0.8° N– 4.0° N) are separated by a low coupled area, hereafter referred to as the Punta Galera-Mompiche Zone (PGMZ). Large interplate earthquakes repeatedly occurred within the coupled zones in 1958 (Mw 7.7) and 1979 (Mw 8.1) for the northern patch and in 1942 (Mw 7.8) and 2016 (Mw 7.8) for the southern patch, while the whole segment is thought to have ruptured during the 1906 Mw 8.4–8.8 great earthquake. We find that during the last decade, the PGMZ has experienced regular and frequent seismic swarms. For the best documented sequence (December 2013–January 2014), a joint seismological and geodetic analysis reveals a six-week-long Slow Slip Event (SSE) associated with a seismic swarm. During this period, the microseismicity is organized into families of similar earthquakes spatially and temporally correlated with the evolution of the aseismic slip. The moment release (3.4×10^{18} Nm, Mw 6.3), over a $\sim 60 \times 40$ km area, is considerably larger than the moment released by earthquakes (5.8×10^{15} Nm, Mw 4.4) during the same time period. In 2007–2008, a similar seismic-aseismic episode occurred, with higher magnitudes both for the seismic and aseismic processes. Cross-correlation analyses of the seismic waveforms over a 15 years-long period further suggest a 2-year repeat time for seismic swarms, which also implies that SSEs recurrently affect this area. Such SSEs contribute to release the accumulated stress, likely explaining why the 2016 Pedernales earthquake did not propagate northward into the PGMZ.

1. Introduction

At subduction zones, geodetic measurements show that the interseismic coupling (ISC) along the plate interface can be very high, in which case stress accumulates and will most probably be released during large earthquakes, or can be very low, indicating areas at the megathrust slipping at the plate rate (e.g. Scholz, 1998; Chlieh et al., 2008; Perfettini et al., 2010). Between these two extreme behaviors, the ISC maps also image intermediate coupled areas which can be interpreted in several ways. They can reflect actual intermediate slip rate or simply result from the net effect of coupled and uncoupled areas on the subduction interface. The friction heterogeneities along the plate interface provide an explanation for the diversity observed in earthquake sequences and patterns of ISC. Low and intermediate coupled areas, understood as governed by velocity-strengthening behavior (Scholz, 1998), seem to play an important role in the earthquake segmentation, acting as transient or persistent barriers to the seismic rupture

propagation (e.g. Chlieh et al., 2014). More quantitatively, dynamic models show that the ability of velocity-strengthening areas to stop the seismic rupture propagation depends on their width and coupling level (Kaneko et al., 2010).

Geodetic observations have also revealed another stress release process, referred to as Slow Slip Events (SSE), characterized by days-to-months long episodes of aseismic slip. This type of phenomena has now been reported worldwide in both subduction and continental fault settings (Linde et al., 1996; Cervelli et al., 2002; Segall et al., 2006; Lohman and McGuire, 2007; Hirose et al., 1999; Dragert et al., 2001; Ozawa et al., 2002; Ozawa et al., 2003; Obara and Hirose, 2005; Douglas et al., 2005; Ohta et al., 2006; Schwartz and Rokosky, 2007; Outerbridge et al., 2010; Vallée et al., 2013). The SSEs show a great variability in duration, extent, equivalent magnitude, depth and slip propagation velocities (e.g., Schwartz and Rokosky, 2007; Peng and Gombert, 2010; Gao et al., 2012). SSEs are usually accompanied by seismic tremors (e.g., Obara, 2002; Rogers and Dragert, 2003), very

* Corresponding author at: Instituto Geofísico-Escuela Politécnica Nacional, Quito, Ecuador.
E-mail addresses: svaca@igepn.edu.ec, vaca@ipgp.fr (S. Vaca).

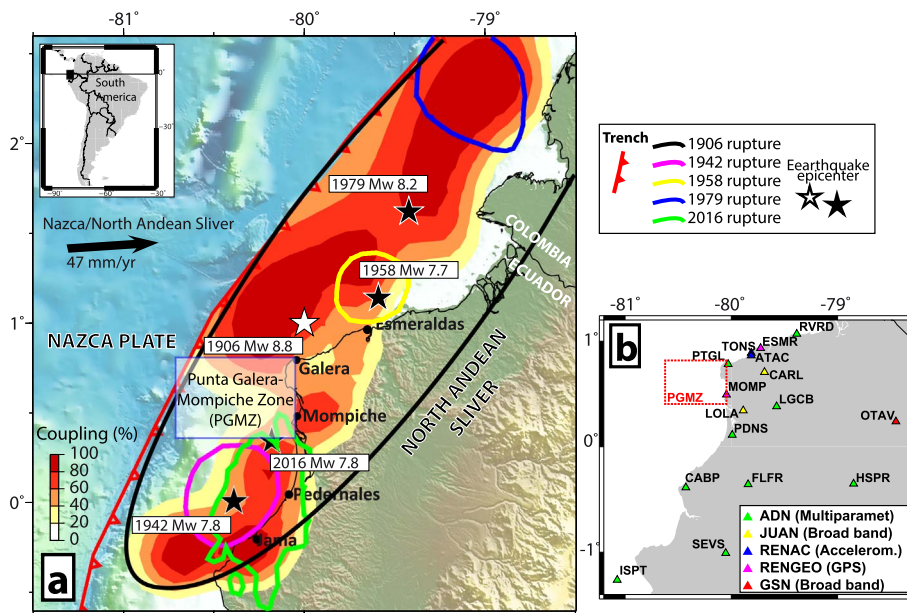


Fig. 1. Location of the Punta-Galera-Mompiche Zone (PGMZ) within the northern Ecuador-southern Colombia subduction zone. a) ISC model (Nocquet et al., 2017), with the estimated main moment release areas (thick-line-contours) for the large earthquakes that occurred in 1906 (Mw 8.4–8.8, Kanamori and McNally, 1982; Okal, 1992; Ye et al., 2016; Yoshimoto et al., 2017), 1942 (Mw 7.8, Swenson and Beck, 1996; Ye et al., 2016; Nocquet et al., 2017), 1958 (Mw 7.7, Swenson and Beck, 1996), 1979 (Mw 8.2 Kanamori and McNally, 1982; Beck and Ruff, 1984) and 2016 (Mw 7.8 Nocquet et al., 2017; He et al., 2017). Stars show the reported epicenters (see text for references). The PGMZ is indicated by the transparent rectangle. b) Map showing the seismic and geodetic stations surrounding the PGMZ (red rectangle) used in this study. (For interpretation of the references to color in this figure legend, the reader is referred to the web version of this article.)

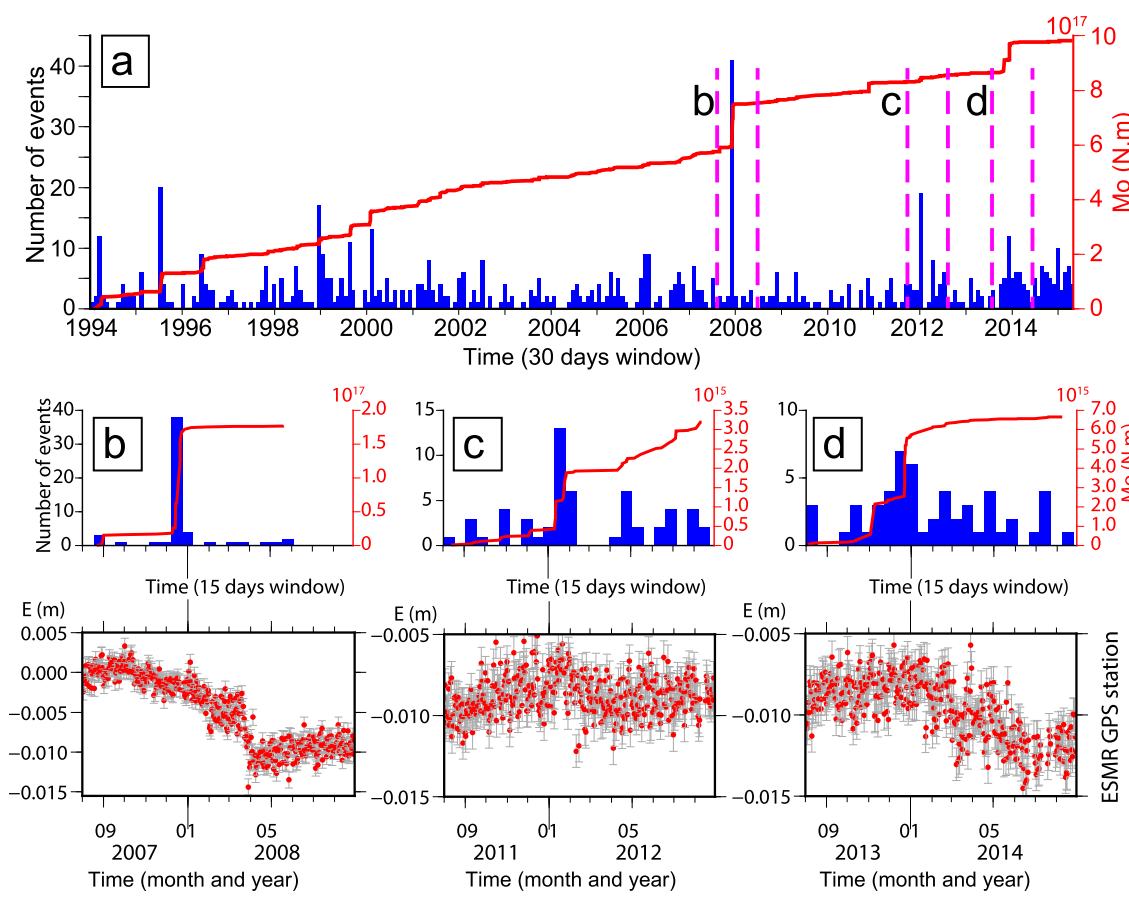


Fig. 2. a) Number of events per month (blue bars) and associated cumulated moment release (red line) for the period January 1994–April 2015 (IG-EPN national catalog). b) Zoom on the December 2007 seismic swarm. Top: number of events (15 days-window) and cumulated seismic moment during the sequence; bottom: eastward displacement recorded by the ESMR GPS station in the same time period. c) and d) Same as b) for the December 2011–January 2012 and November 2013–February 2014 seismic swarms, respectively. (For interpretation of the references to color in this figure legend, the reader is referred to the web version of this article.)

low-frequency earthquakes (e.g. Shelly et al., 2006; Bostock et al., 2012; Frank et al., 2013) and sometimes by high-frequency earthquakes having a swarm character (e.g. Sagiya, 2004; Ozawa et al., 2007; Wallace et al., 2012; Hirose et al., 2014; Vallée et al., 2013). A lot of attention has been paid to study and understand these phenomena,

because SSEs can potentially influence the genesis and evolution of earthquakes ruptures (e.g. Kato et al., 2012; Uchida and Matsuzawa, 2013; Yokota and Koketsu, 2015; Kato et al., 2016). For example, in the Guerrero subduction zone in Mexico, SSEs release a significant fraction of interseismic strain build up (Gualandi et al., 2017) and also trigger a

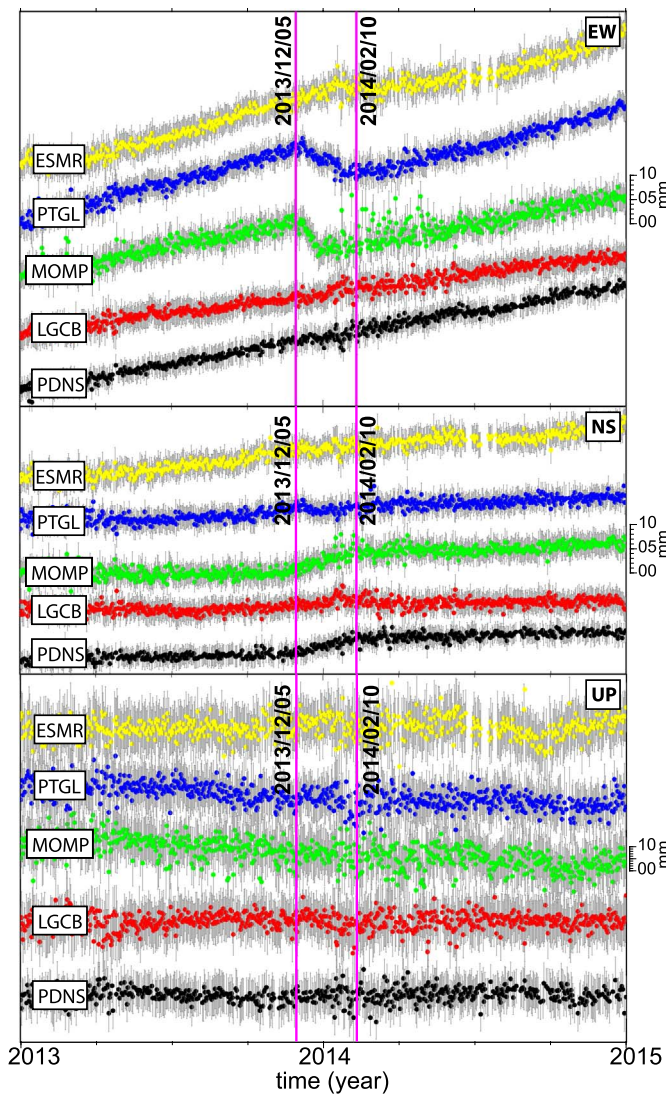


Fig. 3. Three-component GPS time series between 2013 and 2015 (see map of the stations in Fig. 1). On the right side of each component, the scales represent the amplitude in mm of the GPS displacements. The magenta vertical lines delimit the period of the detailed GPS analysis (Section 3.3). (For interpretation of the references to color in this figure legend, the reader is referred to the web version of this article.)

nearby large earthquake (Radiguet et al., 2016).

Here, we focus on an area located in northern Ecuador, referred hereafter to as the Punta Galera-Mompiche Zone (PGMZ). In Ecuador, the Nazca plate converges toward the South America continent at a velocity of 58 mm/yr (Kendrick et al., 2003). Part of this convergence is accommodated by the northeastward motion (~9–10 mm/yr) of the North-Andean Sliver (NAS), resulting in a slip rate of ~47 mm/yr at the megathrust (Nocquet et al., 2014) (Fig. 1). The PGMZ marks the transition between two highly locked areas at the megathrust (Fig. 1), namely the Jama-Pedernales segment between latitudes 0.4°S and 0.35°N, and the Esmeraldas-Buenaventura segment from latitudes 0.8°N to 4.0°N. Both segments are thought to have ruptured during the great 1906 earthquake (Mw 8.4–8.8, Kanamori and McNally, 1982; Okal, 1992; Ye et al., 2016; Yoshimoto et al., 2017). Large earthquakes (Mw 7.7–8.2) have later broken individually both the northern segment in 1958 and 1979 (Kanamori and McNally, 1982; Beck and Ruff, 1984; Swenson and Beck, 1996) and the southern segment in 1942 and 2016 (Swenson and Beck, 1996; Nocquet et al., 2017; Ye et al., 2016; Yoshimoto et al., 2017; He et al., 2017). This context of heterogeneous coupling, associated with the occurrence of large earthquakes,

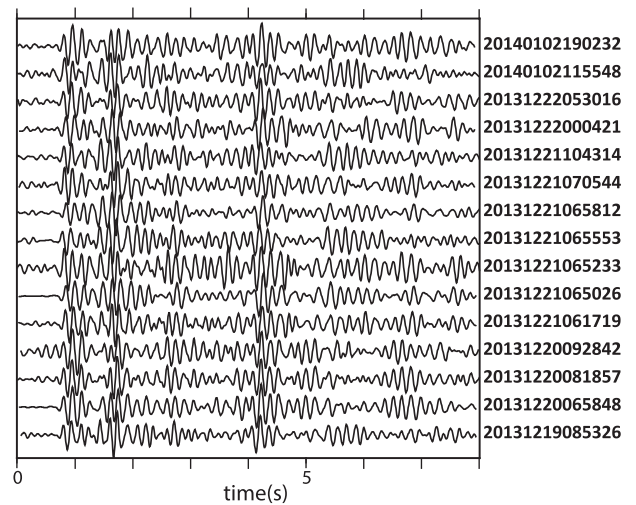


Fig. 4. Example of a family with 15 similar events detected by waveform cross-correlation. Date of each event is indicated to the right in the format year (4 numbers), month, day, hour, minute, second (two numbers).

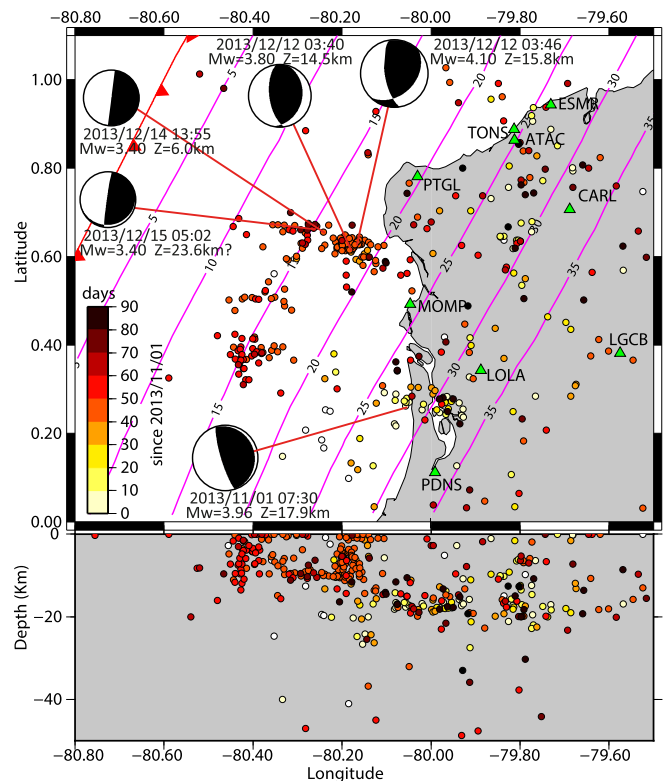


Fig. 5. Location in map view (top) and East-West cross-section (bottom) of the seismicity between 2013/11/01 and 2014/01/31. Color scale represents the day of occurrence since 2013/11/01. Green triangles are the seismic and accelerometric stations used in the location and focal mechanism analyses. Focal mechanisms and source parameters of the five earthquakes analyzed with the MECAVEL method are shown. The labeled pink lines show depth contours (in km) of the subduction interface (Hayes et al., 2012) and the red line with triangles indicates the trench location. (For interpretation of the references to color in this figure legend, the reader is referred to the web version of this article.)

motivates a thorough study of the stress accumulation and release processes at work in the PGMZ. Here, we combine geodetic and seismic analyses in order to document the seismic and aseismic behavior at the PGMZ. We first summarize the available information about the deformation processes in the PGMZ, and then specifically investigate a well recorded seismic-aseismic sequence that occurred in 2013–2014. We next explore how often SSEs occur at the PGMZ, using the 15-year-

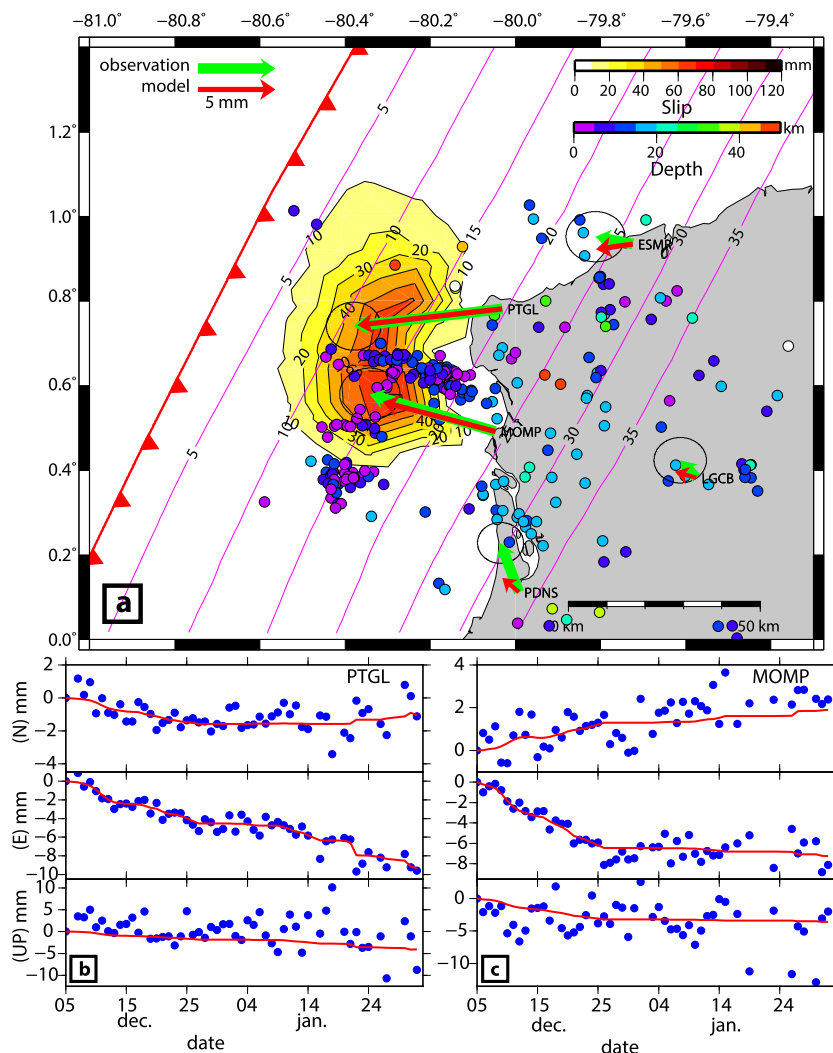


Fig. 6. Time-dependent inversion of slip during the SSE. a) Preferred solution ($\sigma = 50$, $D_c = 40$) for the total slip during the SSE. Observed displacements (with their 95% confidence level error ellipses) and synthetics are shown by green and red arrows respectively. The amount of slip is indicated by the color scale at the top-right. Color dots are the earthquakes located in this study, coded according to the depth color scale. The red and pink lines represent the trench and the iso-depth contours of the interface, respectively. Note the spatial correlation between the southern patch of high slip and seismicity. b) and c) Observed (blue dots) and modeled (red curve) three-component GPS time series at PTGL and MOMP sites. (For interpretation of the references to color in this figure legend, the reader is referred to the web version of this article.)

long continuous records from the OTAV seismic station from the IRIS IU network. These observations are finally used to interpret the segmentation of subduction earthquakes in Ecuador and its relationship with the recent Mw 7.8, 2016 Pedernales earthquake.

2. Seismic swarms and SSEs in the PGMZ before 2013

Inside and around the PGMZ, the earthquake catalog from the Instituto Geofísico, Escuela Politécnica Nacional (IG-EPN), has reported since 1994 frequent peaks of seismicity with a swarm character. Nine seismic swarms (July 1995, June 1996, December 1998, February–April 2000, January 2002, January 2006, December 2007, December 2011–January 2012 and November 2013–February 2014), were characterized by low to moderate magnitude earthquakes (Fig. 2b–d). The progressive development of the geodetic and seismic continuous networks has provided more information through time. The first GPS station (ESMR, close to the city of Esmeraldas, Fig. 1), installed in 2007, recorded a clear trenchward transient signal of 13 mm between October 2007 and March 2008 (Mothes et al., 2013). The smooth reverse displacement observed at the beginning gradually steepens at the end of this period, possibly due to the slow slip migrating closer to the ESMR-station site. During this period, an increased seismicity rate is noted from the end of November to mid-December 2007. The largest earthquake of Mw 5.1, with a thrust mechanism (Global Centroid-Moment-Tensor, Ekström et al., 2012) is consistent with a slip along the subduction interface. It occurred in the middle of the sequence, a typical

characteristic of a seismic swarm (Holtkamp and Brudzinski, 2011). Other events with a magnitude > 4.5 were reported (IG-EPN) and the total moment release during this seismic swarm was close to 1.6×10^{17} Nm (Mw 5.4).

Another seismic swarm occurred from December 2011 to January 2012 (Fig. 2c) with lower magnitude earthquakes (maximum magnitude of 4.0), leading to a total seismic moment release $\sim 1.6 \times 10^{15}$ Nm (Mw 4.1) (Fig. 2c). The small transient observed at ESMR (Fig. 2c) is too close from the noise to assert the presence of a slow slip process and no convincing reversal signals were detected neither for this period at any of the GPS stations PTGL, MOMP, PDNS (see Fig. 1b for GPS sites location).

3. The 2013–2014 sequence

The analysis of this sequence benefits from both the permanent national GPS/seismic network and a temporary seismic network installed around the PGMZ (Fig. 1b). The whole network includes 9 multi-parameter stations (broad band seismometer, accelerometer and GPS from the ADN Project), two broad band seismometers from a temporary network (JUAN project), three accelerometers and two GPS stations from the Ecuadorian national GPS network (Fig. 1b).

3.1. First-order geodetic and seismic characteristics

The horizontal GPS time series at two stations (MOMP, PTGL) show

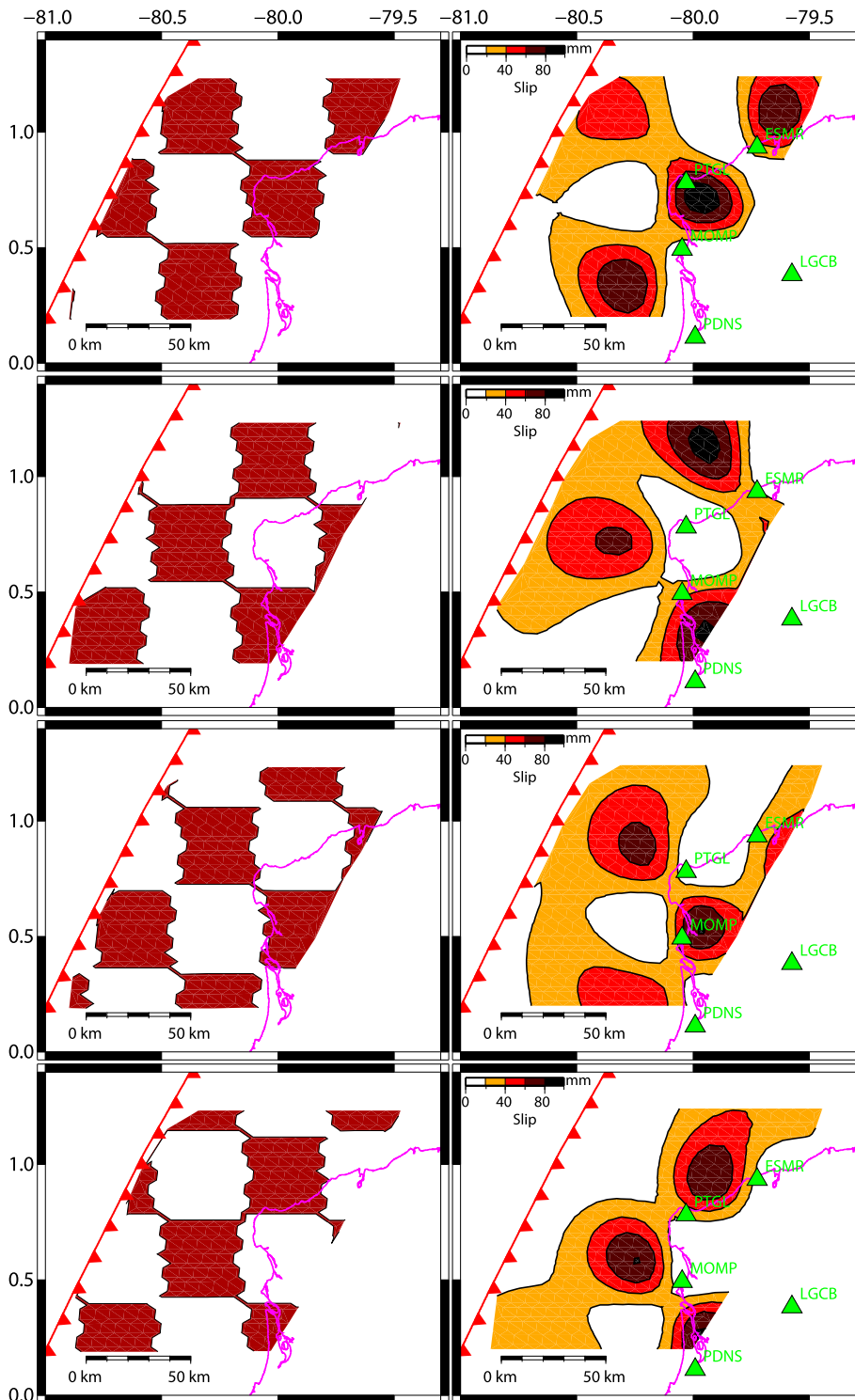


Fig. 7. Checkerboard results for a simulation using $40 \times 40 \text{ km}^2$ patches with 60 mm slip. The left and right panels are the input and retrieved slip distributions, respectively. Each row considers different locations of the slip patches on the subduction interface.

a clear $\sim 1 \text{ cm}$ westward transient displacement over a two-month period (Fig. 3), providing a direct evidence for an SSE. The signals are smaller on the North-South component, as expected in the case of a thrust movement along the subduction interface, but can be clearly seen at PDNS and MOMP stations (0.5 cm northward). Vertical components for all the GPS stations do not show evidences of motion. Because of the higher noise level compared to the horizontal components, this observation only constrains the vertical displacement to be below $\sim 1 \text{ cm}$ at all stations.

The IG-EPN catalog reports 20 earthquakes with magnitudes

between 3.0 and 4.1 during these two months, with a main activity occurring between 2013/12/11 and 2013/12/21 (Fig. 2). The 14 events recorded during this 10 day-long period contrasts with the 31 events recorded during the whole year preceding the SSE. This preliminary seismic observation suggests that the seismic activity was driven by the SSE, as also observed in central Ecuador (Vallée et al., 2013), Japan (Sagiya, 2004; Hirose et al., 2014), and New-Zealand (Wallace et al., 2012) subduction zones.

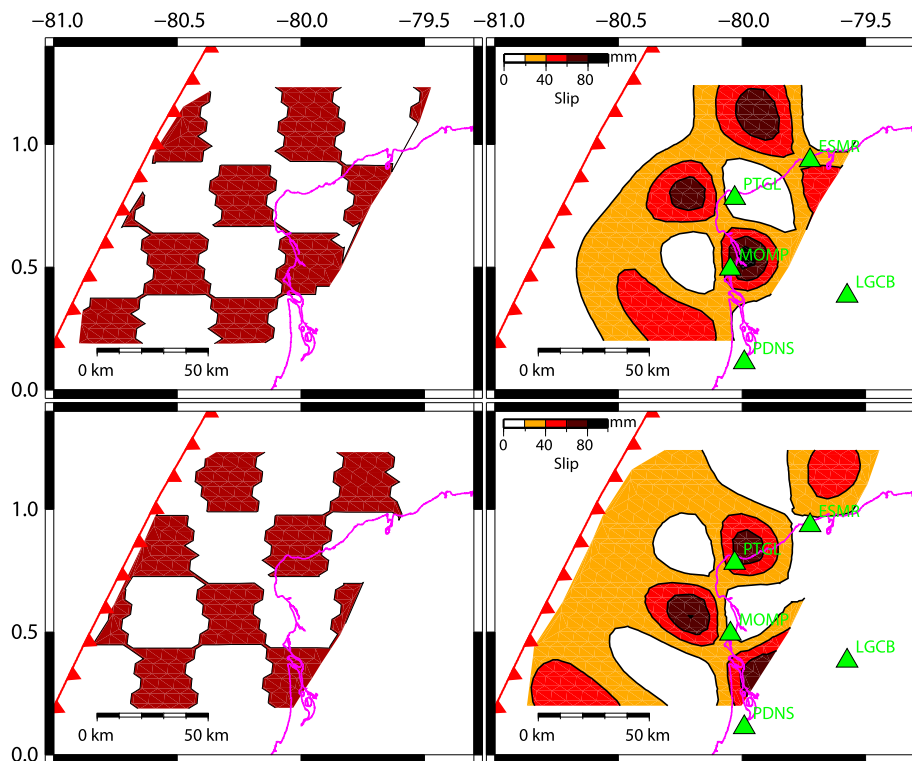


Fig. 8. Checkerboard results for a simulation using $30 \times 30 \text{ km}^2$ patches with 60 mm slip. The left and right panels are the input and retrieved slip distributions, respectively. Each row considers different locations of the slip patches on the subduction interface.

3.2. Micro-seismicity characteristics

3.2.1. Cross-correlation and classification into families of similar earthquakes

During a slow slip process, the surrounding medium is continuously and increasingly stressed. The repeated seismic activation of earthquake-prone areas is therefore an indicator of such a process. The cross-correlation (CC) techniques offer a way to track similar sources and more generally to make a classification of the seismicity (Everitt et al., 2011). In order to identify similar events, we apply a classification algorithm based on CC (Battaglia et al., 2003) to events which were visually identified and extracted from the continuous vertical seismograms of the LOLA broadband seismic station (see Fig. 1b for location). Data from this station are optimal in terms of signal-to-noise ratio and distance to the sources. A total of 1483 single events, with S-P values $< 12 \text{ s}$ (epicenter $< 100 \text{ km}$ from the LOLA station) were extracted during the period between 01/11/2013 and 31/01/2014. Cross-correlations are computed using 8.2 s-long time windows (long enough to include P and S phases for events in the PGMZ), after filtering the signals between 6 and 16 Hz. In this high frequency range, the signals are clear for events with magnitudes as low as 1.9. A given event is considered to belong to a family if it has a normalized CC value greater or equal to 0.7 with at least one event from a given family. This level of waveform similarity requires that the sources have close locations and similar focal mechanism.

Using these parameters, 361 events were grouped into 46 families including 4 to 34 elements (Fig. 4). The events of each family are then stacked in order to obtain templates, which we subsequently use to search by cross-correlation for possibly undetected similar events in the three-month long continuous data. However, this exhaustive scan did not result in the detection of additional family members, probably because all signals above the signal-to noise ratio had already been manually extracted. This cross-correlation procedure first shows that part of the seismicity tends to be spatially clustered, rather than diffused. Additionally, it indicates that small fault patches were repeatedly, or progressively, ruptured during the SSE, in agreement with an incremental stress process.

3.2.2. Seismic location and waveform inversion

In order to determine the location of this clustered seismicity, we use the arrival times recorded at the nearest seismic stations and accelerometers (Figs. 1, 5). We use the DEPNET algorithm (Régner, pers. comm.) for manual picking and the module NETLOC (Régner, pers. comm.) to compute locations. The latter method uses a nonlinear grid search algorithm to find the hypocenter and the origin time of the earthquakes. We use a 1D velocity model optimized for the PGMZ area. As a lot of earthquakes have low magnitudes with onsets close to the noise level, only $\sim 30\%$ (430 earthquakes) of the events detected at the LOLA station could be reliably located using at least four P-phases and one S-phase. For these events, the average root mean square of the time residuals is $\sim 0.07 \text{ s}$. Because of the low azimuthal coverage with respect to the seismicity area, mostly located offshore, depths could not be precisely determined (cross section of Fig. 5). The offshore seismicity, which represents $> 50\%$ of the located earthquakes, shows two trends aligned in the WNW-ESE direction (at latitudes 0.4°N and 0.7°N), approximately perpendicular to the trench (Fig. 5). Font et al. (2013) found a similar spatial distribution, after a 3D relocation of the seismicity recorded by the national network between 1994 and 2007. Similarly, Pontoise and Monfret (2004), using data from a temporary offshore-onshore network, obtained the same trend. These two seismic alignments are separated by a $\sim 30 \text{ km}$ wide gap and a smaller cluster is observed between them. The onshore seismicity is sparser, even if it is closer from the stations, and can be considered as background seismicity.

The focal mechanisms of the offshore seismicity could be determined by waveform inversion for the five largest earthquakes of the swarm. We use the MECAVEL method (described in Grandin et al., 2017), which optimizes the source parameters (double couple focal mechanism, hypocentral location and moment magnitude M_w) simultaneously with a simple velocity model. Optimization is based on the minimization of the residuals between observed and synthetic 3D displacement waveforms, typically filtered between 0.03 Hz and 0.06 Hz. The inverted focal mechanisms show reverse slip on fault planes with North-South azimuths, dipping with low angles to the East (Fig. 5). Focal depths range between 6 and 18 km (except for the event

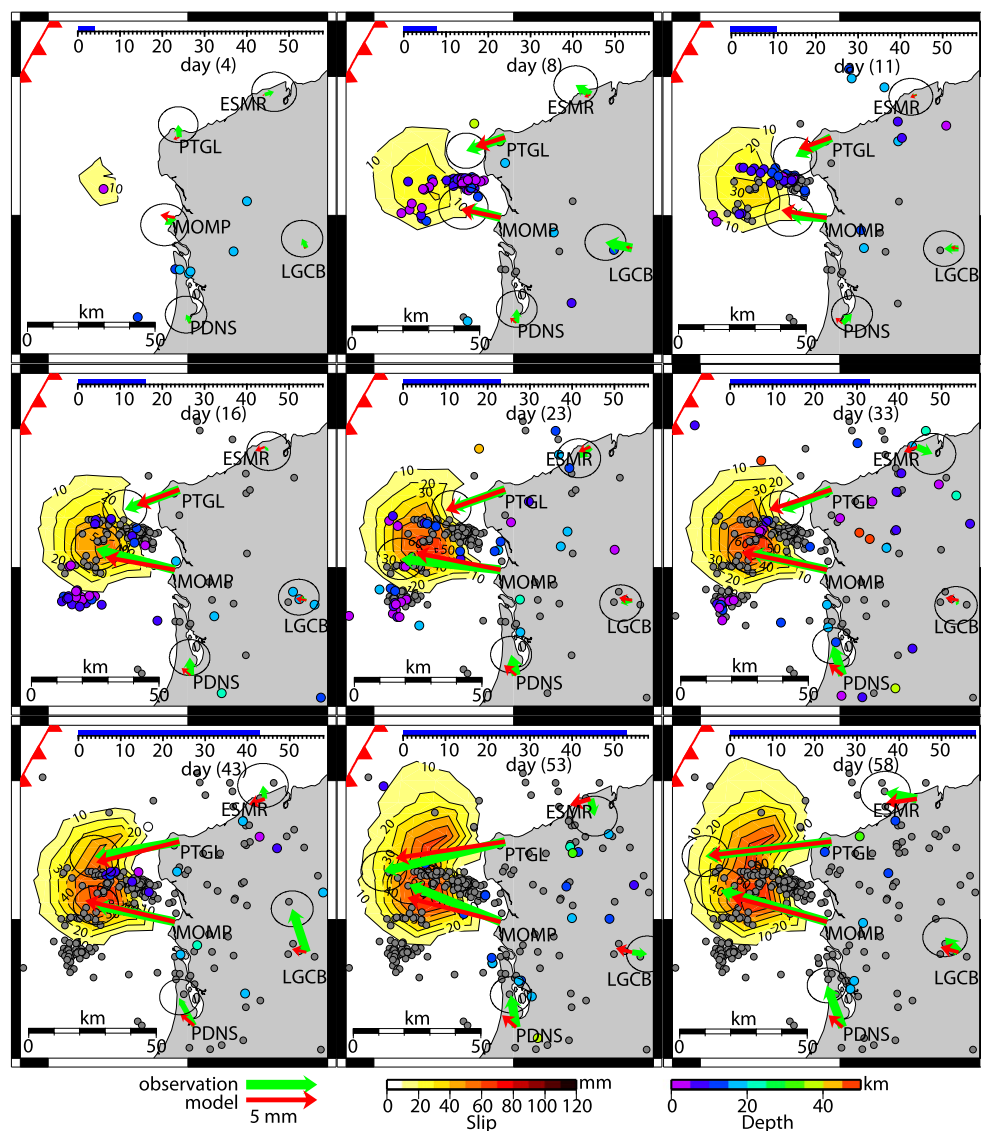


Fig. 9. Space-time evolution of slow slip and seismicity. Each sub-figure shows the cumulated slip (color scale at the bottom of the figure) at the date indicated at the top of each sub-figure. Day 01 is here 2013/12/05. Observed (green arrows, with their 95% confidence level error ellipses) and modeled (red arrows) GPS displacements are shown for each time step. Earthquakes occurring since the previous time step are shown with colored dots (according to depth), and grey dots correspond to the past seismicity since 2013/12/05. The minimum magnitude of the located earthquakes is 1.7 (for some events inside the network). The trench is indicated by the red line with triangles. (For interpretation of the references to color in this figure legend, the reader is referred to the web version of this article.)

2013/12/15 05:02 for which the depth is not well resolved) and deepens to the East. These results are consistent with a thrust motion along the subduction interface. The largest earthquake has a seismic moment of 1.7×10^{15} Nm (M_w 4.1), and the total moment release of the five largest earthquakes is $\sim 4.0 \times 10^{15}$ Nm ($M_w \sim 4.4$). Using a simple magnitude conversion (from ML to M_w) for the smaller events, the total moment for the whole detected seismicity is estimated to be $\sim 5.8 \times 10^{15}$ Nm ($M_w \sim 4.4$).

3.3. Time-dependent inversion of slip from GPS time series

Continuous GPS data for Ecuador (Mothes et al., 2013) were processed together with 48 sites from the global network of the International GNSS Service for Geodynamics (<http://www.igs.org>), using the GAMIT/GLOBK software (Herring et al., 2015) to derive daily loosely constrained solutions. Time series expressed in the ITRF2008 (Altamimi et al., 2011) were first obtained using a 7-parameter transformation with respect to the cumulative solution from the IGS updated up to March 2016. The obtained time series show regionally coherent variations at a scale of several hundreds of kilometers as commonly found in GPS analysis (e.g. Wdowinski et al., 1997). Such variations reflect reference effects and/or the elastic response of the Earth to mass redistribution in continental water, the ocean and the atmosphere (e.g.

Dong et al., 2002), not related to the signal investigated here. In order to remove these effects, we define a local reference frame using 5 CGPS sites located ~ 200 km surrounding the PGMZ zone for which a position at the reference epoch 2014.0 and velocities in a North Andean Sliver (Nocquet et al., 2014) co-moving frame are estimated. Such a reference frame provides the time series with respect to the overriding plate and removes the seasonal and higher frequency regional common mode motion (Williams et al., 2004). In order to extract the signal associated to the SSE, we estimate a trend and a position at a reference epoch using all data available but excluding the SSE period where we solve for an offset. The displacements used as input for subsequent modeling are the residuals with respect to this model, together with their formal errors, that have been rescaled so that they are consistent with the short-term repeatability.

We use a curved geometry for the subduction interface based on the Slab1.0 model for South-America (<http://earthquake.usgs.gov/data/slab/>, Hayes et al., 2012), discretized into 138 triangular subfaults, from 0.30° N to 1.4° N in latitude and from the trench down to 25 km depth. We fixed the rake to 125° consistent with the focal mechanisms at the PGMZ and the Nazca plate/North Andean sliver relative motion. We calculate the transfer function relating the unit slip in the rake direction at each subfault to the displacement components at the GPS sites using Okada (1992) formulas. The inversion strategy follows an

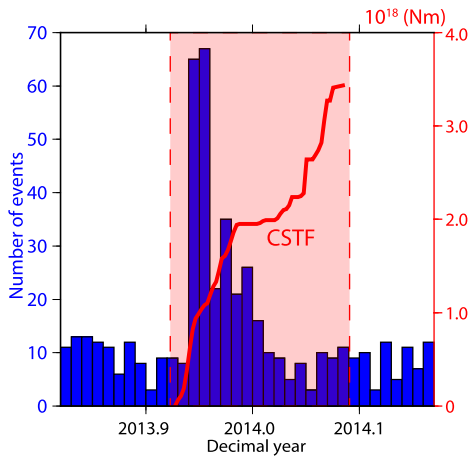


Fig. 10. Cumulated source time function (CSTF) of the 2013–2014 SSE obtained from geodetic inversion (red curve), compared with seismicity activation (histogram of number of events in 0.01 year (3.65 days) time windows). The time window of the histogram starts on 2013.85 (2013/11/07) and ends on 2014.15 (2014/02/24), and therefore corresponds to a longer period than the one shown in Fig. 9. However, inside the red colored rectangle coinciding with the period of occurrence of the SSE, the seismicity activation corresponds to the earthquakes shown in Fig. 9 (magnitude range between 1.7 and 4.1). (For interpretation of the references to color in this figure legend, the reader is referred to the web version of this article.)

approach where the slip increment at each subfault between two successive dates of the GPS dates is solved using least-squares with a non-negativity constraint (Stark and Parker, 1995). Regularization constraints are imposed by the way of a model covariance matrix controlling the level of damping and smoothing with respect to an a priori model (Tarantola, 2005; Radiguet et al., 2011; Nocquet et al., 2014) here taken as 0. The covariance matrix is taken as an isotropic decreasing exponential:

$$Cm_{ij} = \sigma^2 \exp(-d_{ij}/Dc)$$

where Cm_{ij} are the model covariance matrix elements corresponding to the i^{th} and j^{th} subfaults, σ a constant (unit in mm) controlling the weight of the regularization, d_{ij} the distance between the center of subfaults i and j , and Dc is a correlation length controlling the level of spatial smoothing. No temporal smoothing is added here aside the non-negativity constraint imposing that slip must grow through time. In this approach, decreasing values of σ and increasing values of Dc provide smoother models (Supplementary Fig. S1). Based on Fig. S1, we use a 2D L-curve criterion (Hansen, 1992) to choose the smoothest model explaining the GPS data, corresponding to $\sigma = 50$ mm and $Dc = 40$ km

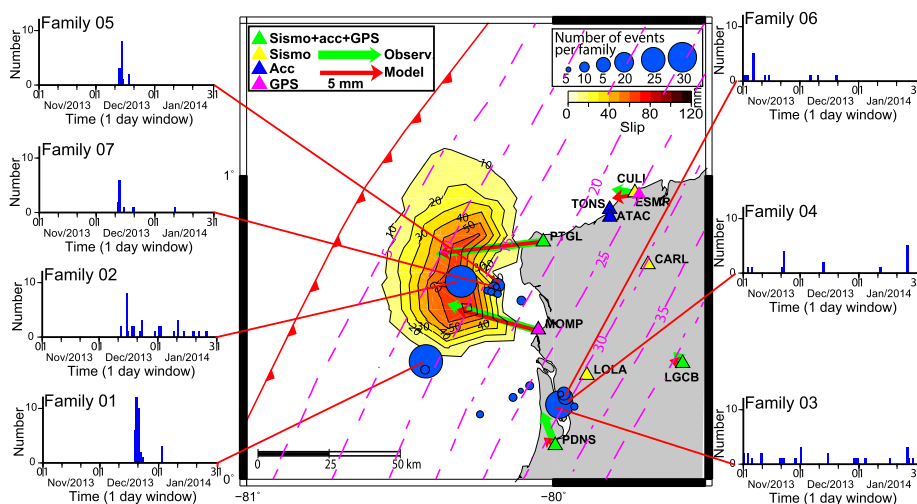


Fig. 11. Space-time relationship between slow slip and families activation. The location of the seven most populated families are shown on the map (with circles scaled to the number of events as shown in the top-right corner) and a corresponding activation histogram is shown for each of these families. Offshore families (1, 2, 5 and 7) can be understood as triggered by the SSE slip gradients, while those inland likely represent a regular background seismicity in the region. Locations of other less populated families are also shown on the map. The red and pink lines represent the trench and the iso-depth contours of the interface, respectively. (For interpretation of the references to color in this figure legend, the reader is referred to the web version of this article.)

(Fig. 6a) and providing a weighted root mean square (wrms) of the residuals of 0.6 mm on the horizontal components (Fig. 6b, c). Vertical GPS time series are included in this inversion (with an uncertainty of 10 mm) but results are not affected if using only the horizontal components (Fig. S2).

The kinematic inversion indicates an initiation on December 9, 2013 starting ~ 40 km west of Mompiche site (MOMP), corresponding to a shallow depth of ~ 15 km (Fig. 9). The rupture then propagates mostly by growing around the initiation point during a month. In a second phase starting in January, a northward propagation of the slip is suggested by the GPS displacements with an increasing northward component observed at the two closest coastal sites. The development of slip in the northern part offshore in front of GPS site PTGL lasts about four weeks, during which the southern patch still seems to continue to slip, but at a slower rate than during the first month. We estimate the average propagation for the whole process to be around ~ 1 km/day in the northern direction. This value is of the same order as the SSEs velocities compiled in Gao et al. (2012) and as the ones reported for the 2010 SSE in Central Ecuador (Vallée et al., 2013).

The resulting slip distribution draws an elongated shape with an approximately North-South direction, having ~ 70 km for the longer axis and ~ 40 km E-W direction. The maximal computed displacement is ~ 75 mm near the initiation region (Figs. 6, 9). The moment released estimated from the GPS data is 3.4×10^{18} Nm leading to an equivalent moment magnitude of Mw 6.3. The SSE cumulative source time function (Fig. 10) separates the two principal phases mentioned previously.

We assess the resolution of our inversion by performing checkerboard tests. The checkerboard tests are performed for a static inversion. Each patch area involves 60 mm of slip, a slip amount similar to the average slip found in our inversion. A formal error corresponding to the one found for the true GPS data is given to the synthetic displacements in the inversion. For each test, we use the two-dimensional L-curve to find the smoothest model explaining the GPS data. Because checkerboard test results may vary depending on the location of the slip patches, we perform various tests with different locations of the patches (Figs. 7, 8). Despite the small number of GPS sites (5), we find that 40×40 km² patches are well resolved from 30 km to 10 km depth at the subduction interface, with the exception of the southern part of the studied area, where the coastline is 80 km away from the trench (Fig. 7). 30×30 km² patches further appear to be resolved close to the coastline (Fig. 8). As a conclusion, the checkerboard tests show that the downslip limit of the SSE is certainly correctly determined. The good resolution obtained at the places where we observe the slip suggest that the slip amount retrieved in our inversion is correct. However, the GPS data offers little control on the slip occurring close to the trench, in particular for the northern patch.

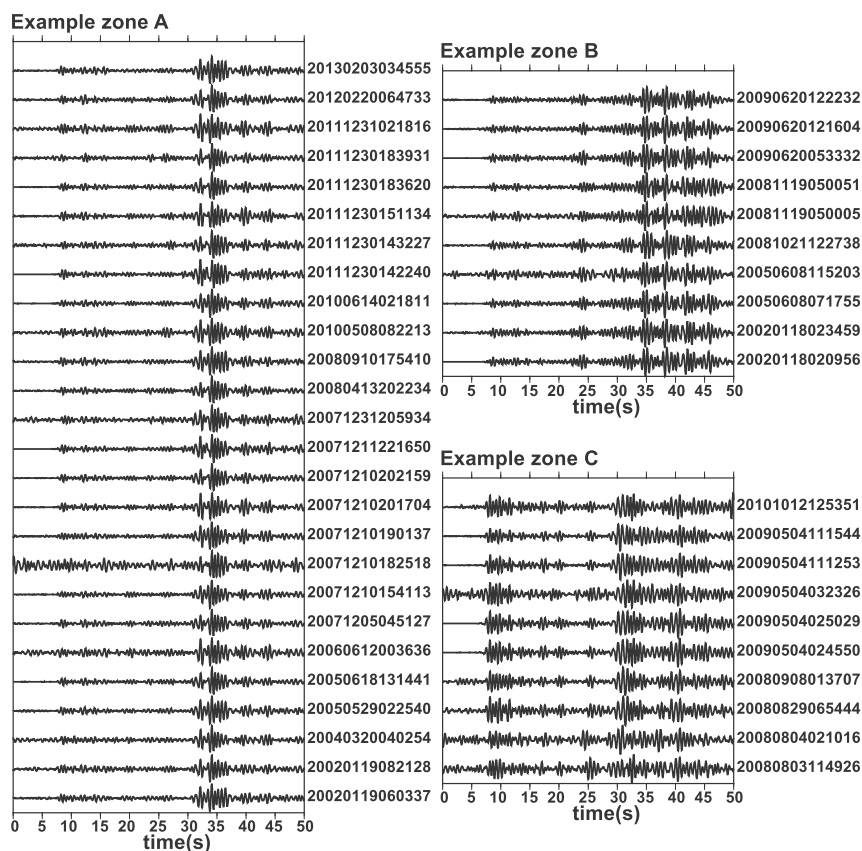


Fig. 12. Examples of family activation revealed by scanning the continuous waveforms of the OTAV station. The three families shown to the left, upper, and lower right are located in the zones A, B and C, respectively (see Fig. 13). The date of each signal, in the format year-month-day-hour-minute-second.

3.4. Relationship between aseismic slip and seismicity

The two phases of the SSE evolution inferred from the GPS time series are associated with two different seismic behaviors. The first phase, characterized by a slip patch growing in size and slip occurs synchronously with a seismic swarm (Figs. 9, 10). The detected seismicity starts a few days after the beginning of the slow slip. Seismicity organized into families of similar earthquakes seems to occur at the slip front rather than in the areas of larger slip. This observation is important to understand the triggering mechanism. Indeed, similar earthquakes appear not to have been triggered by aseismic slip surrounding small asperities. Our results rather suggest that the increment of shear stress at the slip front, where it is the highest, put small asperities to failure, and are then reloaded as slip increases.

The second phase of the SSE corresponds to slip taking place at the northern and western zones of the total slip, at depths shallower than 10 km. This phase occurs almost without any associated seismicity. This absence of seismicity might be explained by the predominance of soft material contained in the accretionary prism at shallower depth close to the trench (Collot et al., 2008; García-Cano, 2009).

Several studies (e.g. Uchida et al., 2016) have proposed to use very similar earthquakes (interpreted as exactly repeating events) as a creep-meter or a proxy for aseismic slip. Here we find that this relation is not direct. Indeed, families of similar earthquakes appear to be active only during the first phase of the SSE. During this period only there is a close space-time relationship between family activation and slow slip process (families 1, 2, 5, 7 in Fig. 11). However, the one-month long second phase of the SSE shows neither seismicity increase nor activation of similar earthquakes. Our exhaustive analysis also detects families of similar earthquakes downdip of the slip area (numbered 3, 4 and 6 in Fig. 11), which are likely poorly correlated with the slow slip process. They are indeed also active before and after the SSE, and can therefore be associated with recurrent background seismicity.

4. Systematic search for other sequences during the 2002–2016 period

We further try to evaluate how frequent SSEs are at the PGMZ by improving the detection of the seismic swarms in the area over a longer time window. To do so, we use the continuous records of the OTAV (www.ds.iris.edu/mda/IU/OTAV) broad-band seismic station from the global network which has data available since 2002. Although OTAV is located in the Andes about 200 km from the PGMZ (see Fig. 13), it is known to be a very good station. We empirically find that OTAV recorded well the events associated with the sequences previously presented.

We first extract the waveforms at OTAV corresponding to the earthquakes located by the national Ecuadorian network (RENSIG) with epicenters inside the PGMZ. This provides 284 waveforms, which we compare pair by pair other using cross-correlation in the 2–4 Hz frequency range. During this first step, 16 families (with 3 to 8 elements) were found. Similar waveforms (cross-correlation coefficient larger than 0.9) are stacked to get an initial set of representative templates. In a second step, the templates are used to scan the continuous data from January 2002 to February 2016 using a relatively low correlation coefficient of 0.7 in order to maximize the number of possible candidates. Finally, in a third step, the found candidates are compared to each other based on a correlation coefficient threshold of 0.9. We finally find 16 families including between 4 and 46 events (Fig. 12).

The temporal distribution of the families shows that throughout the analyzed period, most of the families are activated as swarms during time windows lasting a few days (Figs. 12 and 13). The area named A (see Fig. 13) is of particular interest for the present study as it corresponds to the zone activated during the 2013–2014 sequence. At several times, we observe there a clear synchronous activation for several families, and almost all families are activated at the end of 2007 (Fig. 13). The fact that all families are not active at the same time

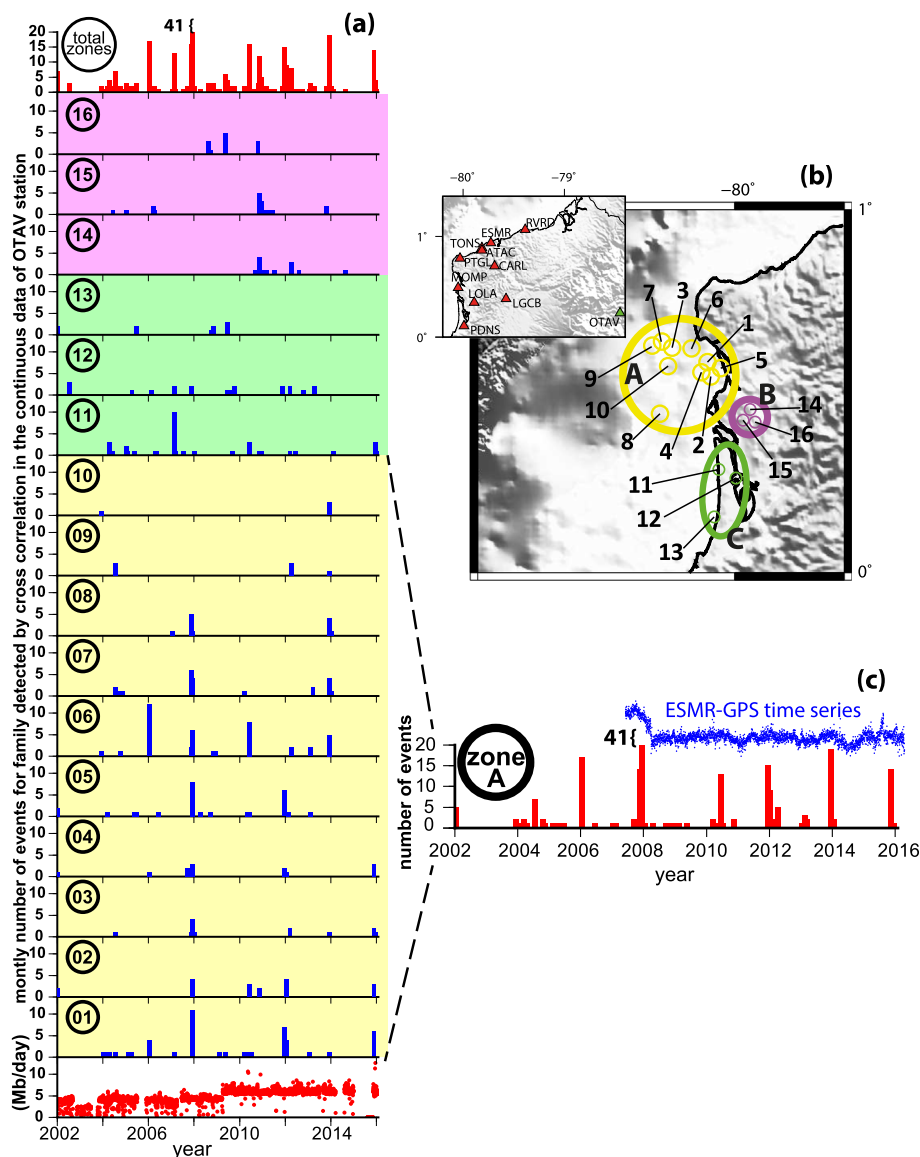


Fig. 13. Family activation and location during the 2002–2016 period. a) Activation histograms of each family and of their combined contributions (first row). The families are classified (yellow, green, and magenta colors) according to the three zones A, B and C shown in the map b). The red points in the last row show the daily file size (mseed format) of the BHZ component of OTAV station and represent the information availability; some steps are due to changes in the response of the seismic instrumentation (www.ds.iris.edu/mda/IU/OTAV). b) Map of the PGMZ showing the location of the families (numbered as in a)) inside the zones A, B and C. The inset shows the location of the OTAV station (green triangle) as well as the stations used for the analysis of the 2013–2014 sequence (red triangles). c) Activation histogram for all the events belonging to families in the zone A. The GPS time series of EMSR (blue dots) show that in 2007–2008 and 2013–2014, geodetic transients and seismicity peaks correlate. (For interpretation of the references to color in this figure legend, the reader is referred to the web version of this article.)

suggests that the PGMZ is affected by transient increases of stress with variable size and location, which trigger different combinations of seismic asperities. When taking into account all the families of the area A (down-left in Fig. 13), a ~ 2 years activation periodicity is observed.

These observations are strong indicators that the PGMZ frequently hosts SSEs having different size and location. The largest SSE for the last 15 years is the 2007–2008 event, which had the largest seismic activity and a geodetic displacement larger than the 2013–2014 event. We interpret the 2010 and 2011–2012 episodes, which are only detected seismically, as being triggered by small SSEs inducing small surface displacements close or below the GPS noise level. An analog of such sequences would be for example the 2001–2002 SSE in western Shikoku (Japan) where only the high sensitivity of tiltmeters could detect the transient change (Obara and Hirose, 2005). Between the large 2007–2008 and the small 2011–2012 SSEs, the 2013–2014 sequence is likely a common case at the PGMZ, indicating that periodic SSEs seismically activate similar patches. This behavior of repeating SSEs of varying size and location has been observed in other subduction segments around the world (e.g. New Zealand, Bartlow et al., 2014) and Boso peninsula (Japan, Ozawa et al., 2008, Hirose et al., 2014) and similar sequences also occurred in Central Ecuador (Vallée et al., 2013; Jarrin, 2015; Segovia, 2016).

5. Relationship with the 2016 Pedernales earthquake

The 2016 Mw 7.8 Pedernales earthquake ruptured a 110 km long and 50 km wide area of the megathrust between 15 and 30 km depth (Nocquet et al., 2017). The earthquake slip distribution abuts the aseismic slip distribution found for the 2013–2014 SSE (Fig. 14). This observation is similar to the results found by Dixon et al. (2014) for the Nicoya Peninsula in Costa Rica, where SSEs outline the co-seismic slip spatial distribution during the Nicoya Mw 7.6 2012 earthquake.

As the PGMZ remained unbroken even if the Pedernales earthquake nucleated immediately next to it (Nocquet et al., 2017), this area can be interpreted as a barrier to the seismic rupture propagation. The PGMZ has a low interseismic coupling and we showed that it regularly hosts SSEs. Both a low interseismic locking and a regular release of slip deficit through SSEs result in a low stress accumulation in this area of the megathrust, when averaged on periods longer than the SSE time recurrence. Taking a range from 20 to 40% of average coupling and an area of $40 \times 40 \text{ km}^2$ (corresponding to the Southern patch of the 2013–2014 SSE), the moment rate deficit being accumulated each year at the PGMZ is $4.7\text{--}9.4 \times 10^{17} \text{ Nm/year}$ or $0.9\text{--}1.8 \times 10^{18} \text{ Nm}$ every two years. These values are similar to the moment released during the 2013–2014 SSE (Fig. 10), resulting in virtually no stress accumulation

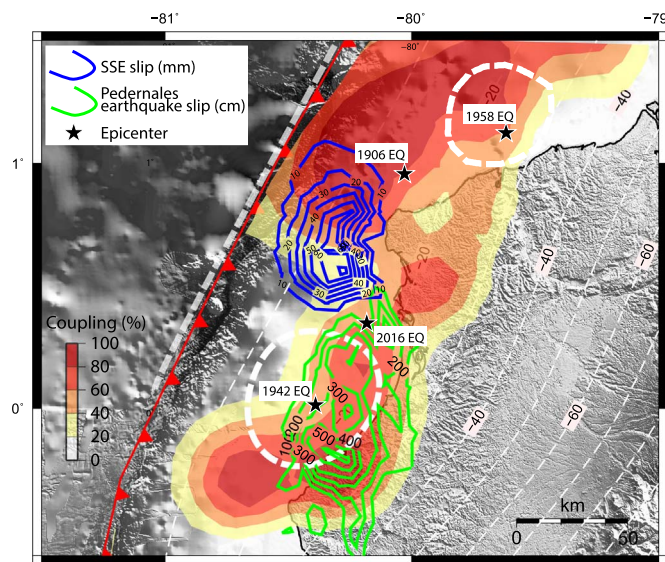


Fig. 14. Seismic and aseismic slip along the central and northern Ecuadorian margin. The ISC model (shown by the color scale) and the 2016 Pedernales coseismic rupture (green contour lines) are taken from Nocquet et al. (2017). Rupture areas of the large 1942 and 1958 earthquakes (Swenson and Beck, 1996) are shown with dashed white lines. Black stars indicate the corresponding epicenters. The slip contours of the 2013–2014 SSE model derived in the present study are shown in blue. (For interpretation of the references to color in this figure legend, the reader is referred to the web version of this article.)

in the PGMZ during the two years preceding the Pedernales earthquake.

Extrapolating this observation prior to 2013 is speculative because the amount of slip release in previous SSEs remains unknown and cannot be inferred from the seismic swarms. Over the 2009–2013 periods, the small 2010 and 2011–2012 SSEs released only a small fraction of the slip deficit accumulated during the same period of time. On the other hand, the 2007–2008 event, with a duration of about 6 months, would correspond to a moment magnitude release of at least Mw 6.7, according to the scaling laws proposed for slow earthquakes (Ide et al., 2007; Gao et al., 2012). Such a magnitude is also consistent with the 12 mm westward displacement observed at ESMR (Fig. 2), located about 50 km from the PGMZ. The 2007–2008 event would have therefore released at least 7 years of slip deficit, suggesting that small SSEs every two years and less frequent larger events release a significant fraction of the slip deficit and accumulated stress in the PGMZ. As a consequence, the PGMZ is an area of stress accumulation lower than what could be inferred from the interseismic coupling map shown in Fig. 14 using 7 years of measurements. Dynamic rupture studies (Kaneko et al., 2010) show that the earthquake propagation is impeded by low-coupled areas, with a probability to act as a barrier depending on their average coupling and size. According to these models, the PGMZ is therefore predicted to be a barrier to the seismic rupture. Furthermore, the barrier role of the PGMZ further appears not to be restricted to the 2016 earthquake. The 1942 earthquake (Fig. 14) shares numerous common properties with the 2016 earthquake (Ye et al., 2016; Nocquet et al., 2017) and among them, its northern extent also appears to have remained confined south of the PGMZ.

As a possible additional interplay between the PGMZ and the Pedernales earthquake, we notice that the 2016 earthquake nucleated in the coupled area of the Jama-Pedernales segment close the PGMZ (Fig. 14). The frequent SSEs occurring at the PGMZ increased the shear stress at their neighboring segments and the hypocentral area has possibly been put closer to failure than the other areas of the Jama-Pedernales coupled patch, that eventually broke during the earthquake.

6. Conclusions

Our study describes the behavior of a small area of the megathrust

whose peculiar properties appear to play an important role in the seismic cycle and earthquake segmentation. Within the PGMZ, seismic swarms occur regularly. Our exhaustive analysis over a 15 year-long time period reveals a recurrence interval of about 2 years. As in other subduction segments, this seismic activity appears to be the response of the medium of the stress increments generated by slow transient aseismic slip along the subduction interface. This finding is supported by two sequences in 2007–2008 and 2013–2014 for which GPS data confirm the contemporaneous occurrence of SSEs with equivalent magnitudes larger than 6.3. For the 2013–2014 sequence, the joint geodetic and seismic data analysis shows a close interplay between slow slip and seismic activation during the first weeks of the two-month long SSE. Seismicity appears to occur close to the borders of the developing slow aseismic slip, supporting the view of a slow-slip zone surrounded by earthquake prone areas which respond to stress increments. The later development of the SSE at shallower depths generates far less seismicity, possibly because frictional properties or softer material of the overriding margin close to the trench impede seismic rupture. We therefore emphasize that seismicity is an efficient tool to track the existence of an SSE, but may not be directly used to quantify its extent.

As shown in Fig. 14, the PGMZ is an area of relatively low interseismic coupling separating two areas with both large earthquake history and stronger coupling. All large past earthquakes of the area, except the great 1906 earthquake, did not cross the PGMZ. Although the ISC within the PGMZ is low, our interpretation is that its efficiency to act as a barrier to seismic rupture is enhanced by the regular occurrence of SSEs, which reduces or even cancels the accumulated stress. In such a configuration, only very rare great events can cross such an unfavorable area.

Acknowledgments

We thank the IRD (Institut de Recherche pour le Développement), the ANR (Agence Nationale de la Recherche, grant ANR-07-BLAN-0143-01 & REMAKE grant ANR-15-CE04-004), the IG-EPN (Instituto Geofísico de la Escuela Politécnica Nacional, Ecuador) and the SENESCYT (Secretaría Nacional de Ciencia y Tecnología of Ecuador, grant PIN-08-EPNGEO-00001: “Fortalecimiento Del Instituto Geofísico”) for their strong support to the project of instrumentation of the Ecuadorian coast (ADN, JUAN projects and the local seismic network). The installation and maintenance of the seismic and geodetic arrays would not have been possible without the help of numerous colleagues from the IRD and IG-EPN. We are also grateful to the SENESCYT for funding of the scholarship for Sandro Vaca’s PhD. The facilities of IRIS Data Services, and specifically the IRIS Data Management Center, were used for access to the OTAV waveforms, related metadata, and/or derived products. Numerical computations were partly performed on the S-CAPAD platform, IPGP, France. Comments and ideas given by M. Segovia were valuable for this study. The careful reviews provided by two anonymous reviewers and by the Editor (J.-P. Avouac) largely contributed to improve the initial versions of the manuscript.

Appendix A. Supplementary data

Supplementary data to this article can be found online at <https://doi.org/10.1016/j.tecto.2017.12.012>.

References

- Altamimi, Z., Collilieux, X., Métivier, L., 2011. ITRF2008: an improved solution of the international terrestrial reference frame. *J. Geod.* 85 (8), 457–473. <http://dx.doi.org/10.1007/s00190-011-0444-4>.
- Bartlow, N., Wallace, L., Beavan, R., Bannister, S., Segall, P., 2014. Time-dependent modeling of slow slip events and associated seismicity and tremor at the Hikurangi subduction zone, New Zealand. *J. Geophys. Res. Solid Earth* 119, 734–753. <http://dx.doi.org/10.1002/2013JB010609>.

- Battaglia, J., Got, J.-L., Okubo, P., 2003. Location of long-period events below Kilauea Volcano using seismic amplitudes and accurate relative relocation. *J. Geophys. Res.* 108 (B12), 2553. <http://dx.doi.org/10.1029/2003JB002517>.
- Beck, S., Ruff, L., 1984. The rupture process of the Great 1979 Colombia earthquake: evidence for the asperity model. *J. Geophys. Res.* 89 (B11), 9281–9291.
- Bostock, M., Royer, A., Hearn, E., Peacock, S., 2012. Low frequency earthquakes below southern Vancouver Island. *Geochim. Geophys. Geosyst.* 13 (11), Q11007. <http://dx.doi.org/10.1029/2012GC004391>.
- Cervelli, P., Segall, P., Johnson, K., Lisowski, M., Miklius, A., 2002. Sudden aseismic fault slip on the south flank of Kilauea volcano. *Nature* 415, 1014–1018. <http://dx.doi.org/10.1038/4151014a>.
- Chlieh, M., Avouac, J.-P., Sieh, K., Natawidjaja, D., Galetzka, J., 2008. Heterogeneous coupling of the Sumatran megathrust constrained by geodetic and paleogeodetic measurements. *J. Geophys. Res.* 113, B05305. <http://dx.doi.org/10.1029/2007JB004981>.
- Chlieh, M., Mothes, P., Nocquet, J.-M., Jarrin, P., Charvis, P., Cisneros, D., Font, Y., Collot, J.-Y., Villegas, J.-C., Rolandone, F., Vallée, M., Regnier, M., Segovia, M., Martin, X., Yepes, H., 2014. Distribution of discrete seismic asperities and aseismic slip along the Ecuadorian megathrust. *Earth Planet. Sci. Lett.* 292–301. <http://dx.doi.org/10.1016/j.epsl.2014.05.027>.
- Collot, J.-Y., Agudelo, W., Ribodetti, A., Marcaillou, B., 2008. Origin of a crustal splay fault and its relation to the seismogenic zone and underplating at the erosional north Ecuador – south Colombia oceanic margin. *J. Geophys. Res.* 113 (B12102), 19. <http://dx.doi.org/10.1029/2008JB005691>.
- Dixon, T., Jiang, Y., Malservisi, R., McCaffrey, R., Voss, N., Protti, M., Gonzalez, V., 2014. Earthquake and tsunami forecasts: relation of slow slip events to subsequent earthquake rupture. *Proc. Natl. Acad. Sci.* <http://dx.doi.org/10.1073/pnas.1412299111>.
- Dong, D., Fang, P., Bock, Y., Cheng, M., Miyazaki, S., 2002. Anatomy of apparent seasonal variations from GPS-derived site position time series. *J. Geophys. Res.* 107 (B4), 2075. <http://dx.doi.org/10.1029/2001JB000573>.
- Douglas, A., Beavan, J., Wallace, L., Townend, J., 2005. Slow slip on the northern Hikurangi subduction interface, New Zealand. *Geophys. Res. Lett.* 32, L16305. <http://dx.doi.org/10.1029/2005GL023607>.
- Dragert, H., Wang, K., James, T.S., 2001. A silent slip event on the deeper Cascadia subduction interface. *Science* 292, 1525–1528. <http://dx.doi.org/10.1126/science.1060152>.
- Ekström, G., Nettles, M., Dziewonski, A., 2012. The Global CMT project 2004–2010: centroid-moment tensors for 13,017 earthquakes. *Phys. Earth Planet. Inter.* 200–201, 1–9. <http://dx.doi.org/10.1016/j.pepi.2012.04.002>.
- Everitt, B., Landau, S., Leese, M., Stahl, D., 2011. *Miscellaneous clustering methods*. In: *Cluster Analysis*, 5th ed. John Wiley & Sons, Ltd., Chichester, UK.
- Font, Y., Segovia, M., Vaca, S., Theunissen, T., 2013. Seismicity pattern along the Ecuadorian subduction zone: new constraints from earthquake location in a 3D a priori velocity model. *Geophys. J. Int.* 193, 263–286. <http://dx.doi.org/10.1093/gji/ggs083>.
- Frank, W., Shapiro, N., Kostoglodov, V., Husker, A., Campillo, M., Payero, J., Prieto, G., 2013. Low-frequency earthquakes in the Mexican Sweet Spot. *Geophys. Res. Lett.* 40, 2661–2666. <http://dx.doi.org/10.1002/grl.50561>.
- Gao, H., Schmidt, D., Weldon, R., 2012. Scaling relationships of source parameters for slow slip events. *Bull. Seismol. Soc. Am.* 102, 352–360. <http://dx.doi.org/10.1785/0120110096>.
- García-Cano, L., 2009. *Imagerie Sismique 3D de la Zone de Subduction à la Frontière Colombie-Equateur*. Thèse. Université de Nice Sophia Antipolis.
- Grandin, R., Vallée, M., Lacassin, R., 2017. Rupture process of the Oklahoma Mw 5.7 Pawnee earthquake from Sentinel-1 InSAR and seismological data. *Seismol. Res. Lett.* 88 (3). <http://dx.doi.org/10.1785/0220160226>.
- Gualandri, A., Nichele, C., Serpelloni, E., Chiaraluce, L., Anderlini, L., Latorre, D., Belardinelli, M., Avouac, J.-P., 2017. Aseismic deformation associated with an earthquake swarm in the northern Apennines (Italy). *Geophys. Res. Lett.* 44. <http://dx.doi.org/10.1002/2017GL073687>.
- Hansen, C., 1992. Analysis of discrete ill-posed problems by means of the L-curve. *SIAM Rev.* 34 (4), 561–580.
- Hayes, G., Wald, D., Johnson, R., 2012. Slab1.0: a three-dimensional model of global subduction zone geometries. *J. Geophys. Res.* 117, B01302. <http://dx.doi.org/10.1029/2011JB008524>.
- He, P., Hetland, E., Wang, Q., Ding, K., Wen, Y., Zou, R., 2017. Coseismic slip in the 2016 Mw 7.8 Ecuador earthquake imaged from sentinel-1A radar interferometry. *Seismol. Res. Lett.* <http://dx.doi.org/10.1785/0220160151>.
- Herring, T., King, R., Floyd, M., McClusky, S., 2015. *Introduction to GAMMIT/GLOBK*. Department of Earth, Atmospheric, and Planetary Sciences, Massachusetts Institute of Technology.
- Hirose, H., Hirahara, K., Kimata, F., Fujii, N., Miyazaki, S., 1999. A slow thrust slip event following the two 1996 Hyuganada earthquakes beneath the Hongo Channel, southwest Japan. *Geophys. Res. Lett.* 26, 3237–3240. <http://dx.doi.org/10.1029/1999GL010999>.
- Hirose, H., Matsuzawa, T., Kimura, T., Kimura, H., 2014. The Boso slow slip events in 2007 and 2011 as a driving process for the accompanying earthquake swarm. *Geophys. Res. Lett.* 41. <http://dx.doi.org/10.1002/2014GL059791>.
- Holtkamp, S., Brudzinski, M., 2011. Earthquake swarms in circum-Pacific subduction zones. *Earth Planet. Sci. Lett.* 305, 215–225. <http://dx.doi.org/10.1016/j.epsl.2011.03.004>.
- Ide, S., Beroza, G.C., Shelly, D., Uchide, T., 2007. A scaling law for slow earthquakes. *Nature* 447, 76–79.
- Jarrin, P., 2015. *Modelamiento de Datos GPS Aplicado al Estudio de la Subducción en el Ecuador*. master report. Escuela Politécnica Nacional, Quito-Ecuador.
- Kanamori, H., McNally, K., 1982. Variable rupture mode of the subduction zone along the Ecuador-Colombia coast. *Bull. Seismol. Soc. Am.* 72, 1241–1253.
- Kaneko, Y., Avouac, J.-P., Lapusta, N., 2010. Towards inferring earthquake patterns from geodetic observations of interseismic coupling. *Nat. Geosci.* 3, 363–369. <http://dx.doi.org/10.1038/NNGEO843>.
- Kato, A., Obara, K., Igarashi, T., Tsuruoka, H., Nakagawa, S., Hirata, N., 2012. Propagation of slow slip leading up to the 2011 Mw 9.0 Tohoku Oki earthquake. *Science* 335, 705–708. <http://dx.doi.org/10.1126/science.1215141>.
- Kato, A., Fukuda, J., Kumazawa, T., Nakagawa, S., 2016. Accelerated nucleation of the 2014 Iquique, Chile Mw 8.2 earthquake. *Nature*. <http://dx.doi.org/10.1038/srep24792>.
- Kendrick, E., Bevis, M., Smalley, R., Brooks, B., Vargas, R., Lauría, E., Fortes, L., 2003. The Nazca-South America Euler vector and its rate of change. *J. S. Am. Earth Sci.* 16, 125–131. [http://dx.doi.org/10.1016/S0895-9811\(03\)00028-2](http://dx.doi.org/10.1016/S0895-9811(03)00028-2).
- Linde, A., Gladwin, M., Johnston, M., Gwyther, R., Bilham, R., 1996. A slow earthquake sequence on the San Andreas Fault. *Nature* 383, 65–68. <http://dx.doi.org/10.1038/383065a0>.
- Lohman, R., McGuire, J., 2007. Earthquake swarms driven by aseismic creep in the Salton Trough, California. *J. Geophys. Res.* 112, B04405. <http://dx.doi.org/10.1029/2006JB004596>.
- Mothes, P., Nocquet, J.-M., Jarrin, P., 2013. Continuous GPS network operating throughout Ecuador. *Eos* 94 (26). <http://dx.doi.org/10.1002/2013EO260002>.
- Nocquet, J.-M., Villegas, J.-C., Chlieh, M., Mothes, P., Rolandone, F., Jarrin, P., Cisneros, S., Alvarado, A., Audin, L., Bondoux, F., Martin, X., Font, Y., Regnier, M., Vallée, M., Tran, T., Beauval, C., Maguñá, J.-M., Matinez, W., Tavera, H., Yepes, H., 2014. Motion of continental slivers and creeping subduction in the northern Andes. *Nat. Geosci.* <http://dx.doi.org/10.1038/ngeo2099>.
- Nocquet, J.-M., Jarrin, P., Vallée, M., Mothes, P., Grandin, R., Rolandone, F., Delouis, B., Yepes, H., Font, Y., Fuentes, D., Régnier, M., Laurendeau, A., Cisneros, D., Hernandez, S., Sladen, A., Singaicho, J.-C., Mora, H., Gomez, J., Montes, L., Charvis, P., 2017. Supercycle at the Ecuadorian subduction zone revealed after the 2016 Pedernales earthquake. *Nat. Geosci.* 10 (2), 145–149. <http://dx.doi.org/10.1038/NNGEO2864>.
- Obara, K., 2002. Nonvolcanic deep tremor associated with subduction in southwest Japan. *Science* 296 (5573), 1679–1681. <http://dx.doi.org/10.1126/science.1070378>.
- Obara, K., Hirose, H., 2005. Non-volcanic deep low-frequency tremors accompanying slow slips in the southwest Japan subduction zone. *Tectonophysics* 417, 33–51. <http://dx.doi.org/10.1016/j.tecto.2005.04.013>.
- Ohta, Y., Freymueller, J., Hreinsdóttir, S., Suito, H., 2006. A large slow slip event and the depth of the seismogenic zone in the south central Alaska subduction zone. *Earth Planet. Sci. Lett.* 247 (1–2), 108–116. <http://dx.doi.org/10.1016/j.epsl.2006.05.013>.
- Okada, Y., 1992. Internal deformation due to shear and tensile faults in a half-space. *Bull. Seismol. Soc. Am.* 82 (2), 1018–1040.
- Okal, E., 1992. Use of the mantle magnitude Mm for the reassessment of the moment of historical earthquakes. *Pure Appl. Geophys.* 139 (1), 17–57. <http://dx.doi.org/10.1007/BF00876825>.
- Outerbridge, K., Dixon, T., Schwartz, S., Walter, J., Protti, M., Gonzalez, V., Biggs, J., Thorwart, M., Rabbel, W., 2010. A tremor and slip event on the Cocos-Caribbean subduction zone as measured by a global positioning system (GPS) and seismic network on the Nicoya Peninsula, Costa Rica. *J. Geophys. Res.* 115, B10408. <http://dx.doi.org/10.1029/2009JB006845>.
- Ozawa, S., Murakami, M., Kaidzu, M., Tada, T., Sagiya, T., Hatanaka, Y., Yari, H., Nishimura, T., 2002. Detection and monitoring of ongoing aseismic slip in the Tokai region, central Japan. *Science* 298 (5595), 1009–1012. <http://dx.doi.org/10.1126/science.107678>.
- Ozawa, S., Miyazaki, S., Hatanaka, Y., Imakiire, T., Kaidzu, M., Murakami, M., 2003. Characteristic silent earthquakes in the eastern part of the Boso Peninsula, central Japan. *Geophys. Res. Lett.* 30 (6), 1283. <http://dx.doi.org/10.1029/2002GL016665>.
- Ozawa, S., Suito, H., Tobita, M., 2007. Spatiotemporal evolution of aseismic interplate slip between 1996 and 1998 and between 2002 and 2004 in Bungo channel, southwest Japan. *J. Geophys. Res.* 112, B05409. <http://dx.doi.org/10.1029/2006JB004643>.
- Ozawa, S., Suito, H., Tobita, M., 2008. Occurrence of quasi-periodic slow-slip off the east coast of the Boso Peninsula, Central Japan. *Earth Planets Space* 59, 1241–1245. <http://dx.doi.org/10.1186/BF03352072>.
- Peng, Z., Gombert, J., 2010. An integrated perspective of the continuum between earthquakes and slow-slip phenomena. *Nat. Geosci.* 3, 599–607. <http://dx.doi.org/10.1038/ngeo940>.
- Perfettini, H., Avouac, J.-P., Tavera, H., Kositsky, A., Nocquet, J.-M., Bondoux, F., Chlieh, M., Sladen, A., Audin, L., Farber, D., Soler, P., 2010. Seismic and aseismic slip on the Central Peru megathrust. *Nat. Lett.* 465, 78–81. <http://dx.doi.org/10.1038/nature09062>.
- Pontoise, B., Monfret, T., 2004. Shallow seismogenic zone detected from an off-shore-onshore temporary seismic network in the Esmeraldas area (northern Ecuador). *Geochim. Geophys. Geosyst.* <http://dx.doi.org/10.1029/2003GC000561>.
- Radiguet, M., Cotton, F., Vergnolle, M., Campillo, M., Valette, B., Kostoglodov, V., Cotte, N., 2011. Spatial and temporal evolution of a long term slow slip event: the 2006 Guerrero Slow Slip Event. *Geophys. J. Int.* 184 (2), 816–828. <http://dx.doi.org/10.1111/j.1365-246X.2010.04866.x>.
- Radiguet, M., Perfettini, H., Cotte, N., Gualandri, A., Valette, B., Kostoglodov, V., Lhommel, T., Walpersdorf, A., Cabral Cano, E., Campillo, M., 2016. Triggering of the 2014 Mw 7.3 Papanao earthquake by a slow slip event in Guerrero, Mexico. *Nat. Geosci.* 9, 829–833. <http://dx.doi.org/10.1038/ngeo2817>.
- Rogers, G., Dragert, H., 2003. Episodic tremor and slip on the Cascadia subduction zone: the chatter of silent slip. *Science* 300, 1942–1943. <http://dx.doi.org/10.1126/science.1084783>.
- Sagiya, T., 2004. Interplate coupling in the Kanto district, central Japan, and the Boso

- Peninsula silent earthquake in May 1996. *Pure Appl. Geophys.* 161, 2601–2616. <http://dx.doi.org/10.1007/s00024-004-2566-6>.
- Scholz, C., 1998. Earthquakes and friction laws. *Nature* 391, 37–42.
- Schwartz, S., Rokosky, J., 2007. Slow slip events and seismic tremor at circum-Pacific subduction zones. *Rev. Geophys.* 45, RG3004. <http://dx.doi.org/10.1029/2006RG000208>.
- Segall, P., Desmarais, E., Shelly, D., Miklius, A., Cervelli, P., 2006. Earthquakes triggered by silent slip events on Kilauea volcano, Hawaii. *Nature* 442, 71–74. <http://dx.doi.org/10.1038/nature04938>.
- Segovia, M., 2016. Imagerie Microsismique d'une Asperité Sismologique dans la Zone de Subduction Équatorienne. Thèse. Université de Nice-Sophia Antipolis - UFR Sciences.
- Shelly, D., Beroza, G., Ide, S., Nakamura, S., 2006. Low-frequency earthquakes in Shikoku, Japan and their relationship to episodic tremor and slip. *Nature* 442, 188–191. <http://dx.doi.org/10.1038/nature04931>.
- Stark, P., Parker, R., 1995. Bounded-variable least-squares: an algorithm and applications. *Comput. Stat.* (10), 129–141.
- Swenson, J., Beck, S., 1996. Historical 1942 Ecuador and 1942 Peru subduction earthquakes and earthquake cycles along Colombia-Ecuador and Peru subduction segments. *Pure Appl. Geophys.* 146, 67–101.
- Tarantola, A., 2005. *Inverse Problem Theory and Methods for Model Parameter Estimation*. SIAM (ISBN 0-89871-572-5 (pbk.)).
- Uchida, N., Matsuzawa, T., 2013. Pre- and postseismic slow slip surrounding the 2011 Tohoku-oki earthquake rupture. *Earth Planet. Sci. Lett.* 374, 81–91. <http://dx.doi.org/10.1016/j.epsl.2013.05.21>.
- Uchida, N., Iinuma, T., Nadeau, R., Bürgmann, R., Hino, R., 2016. Periodic slow slip triggers megathrust zone earthquakes in northeastern Japan. *Science* 351, 488–492. <http://dx.doi.org/10.1126/science.1243108>.
- Vallée, M., Nocquet, J.-M., Battaglia, J., Font, Y., Segovia, M., Régnier, M., Mothes, P., Jarrin, P., Cisneros, D., Vaca, S., Yepes, H., Martin, X., Béthoux, N., Chlieh, M., 2013. Intense interface seismicity triggered by a shallow slow slip event in the Central Ecuador subduction zone. *J. Geophys. Res.* 118, 1–17. <http://dx.doi.org/10.1002/jgrb.50216>.
- Wallace, L., Beavan, J., Bannister, S., Williams, C., 2012. Simultaneous long-term and short-term slow slip events at the Hikurangi subduction margin, New Zealand: implications for processes that control slow slip event occurrence, duration, and migration. *J. Geophys. Res.* 117, B11402. <http://dx.doi.org/10.1029/2012JB009489>.
- Wdowinski, S., Bock, Y., Zhang, J., Fang, P., Genrich, J., 1997. Southern California permanent GPS geodetic array: spatial filtering of daily positions for estimating coseismic and postseismic displacements induced by the 1992 Landers earthquake. *J. Geophys. Res.* 102 (B8), 18057–18070. <http://dx.doi.org/10.1029/97JB01378>.
- Williams, S., Bock, Y., Fang, P., Jamason, P., Nikolaidis, R., Prawirodirdjo, L., Miller, M., Johnson, D., 2004. Error analysis of continuous GPS position time series. *J. Geophys. Res.* 109, B03412. <http://dx.doi.org/10.1029/2003JB002741>.
- Ye, L., Lay, T., Kanamori, H., Rivera, L., 2016. Rupture characteristics of major and great ($M_w \geq 7.0$) megathrust earthquakes from 1990 to 2015: 1. Source parameter scaling relationships. *J. Geophys. Res. Solid Earth* 121, 826–844. <http://dx.doi.org/10.1002/2015JB012426>.
- Yokota, Y., Koketsu, K., 2015. A very long-term transient event preceding the 2011 Tohoku earthquake. *Nat. Commun.* <http://dx.doi.org/10.1038/ncomms6934>.
- Yoshimoto, M., Kumagai, H., Acero, W., Ponce, G., Váscónez, F., Arrais, S., Ruiz, M., Alvarado, A., Pedraza-García, P., Dionicio, V., Chamorro, O., Maeda, Y., Nakano, M., 2017. Depth-dependent rupture mode along the Ecuador-Colombia subduction zone. *Geophys. Res. Lett.* 44, 2203–2210. <http://dx.doi.org/10.1002/2016GL071929>.